Strain Experimental Modal Analysis of an Euler-Bernoulli Beam Based on the Thermoelastic Principle

Klemen Zaletelj[a], Janko Slavič[a,*], Jaša Šonc[a], Miha Boltežar[a]

[a] *University of Ljubljana, Faculty of Mechanical Engineering, Aškerčeva 6, 1000 Ljubljana, Slovenia*

Cite as:
Klemen Zaletelj, Janko Slavič, Jaša Šonc and Miha Boltežar, Mechanical Systems and Signal Processing, Volume 201, 15 October 2023, 110655
https://doi.org/10.1016/j.ymssp.2023.110655

Abstract

The strain mode shapes can be utilized as an indicator of vibration fatigue-hotspots and are utilized for predicting the distribution of damage intensity. However, the conventional approach for measurement, which involves using strain sensors, does not offer the necessary high spatial density required for accurately identifying critical locations or creating a comprehensive map of damage intensity. Non-contact methods have been employed to indirectly determine the full-field strain shapes, but when measuring kinematic quantities, a relation between kinematics and stress/strain must be known. For Euler-Bernoulli beam, the double spatial derivative is required which introduces a significant uncertainty. In contrast, by leveraging the thermoelastic principle, the full-field stress/strain response of an arbitrary structure can be directly measured using a high-speed infrared (IR) camera. The thermoelastic principle has not been extensively researched for strain experimental modal analysis (EMA). In this study, the hybrid EMA (based on one high-dynamic range sensor) was researched for thermoelastic identification of an Euler-Bernoulli beam. The minimum stress/temperature variation required to achieve accuracy comparable to scanning-laser kinematics-based strain

*Corresponding author
Email address: janko.slavic@fs.uni-lj.si (Janko Slavič)

mode shapes was investigated. The findings demonstrate that even when the noise floor is significantly higher than the signal, full-field strain mode shapes can be identified using IR cameras and the hybrid EMA method. By considering the minimum stress/temperature variation determined in this research (for aluminum and steel), the accuracy of thermoelasticity-based strain shapes can be evaluated during the experiment-design stage.
While this research is theoretically and experimentally based on Euler-Bernoulli beam, generalization of the thermoelastic principle to arbitrary structure is feasible.

Keywords: Thermoelastic principle, strain shapes, modal identification, structural dynamics

---

1. Introduction

Strain Experimental Modal Analysis (EMA) [1] is a variant of classical EMA [2] where the strain mode shapes are determined instead of the displacement mode shapes. Based on the strain mode shapes, the fatigue hotspots can be identified and correlated with the critical location on the structure [3]. The results from strain EMA have been directly used in the modal decomposition approach [4], which has been shown to successfully identify the critical point location and damage-intensity distribution. To accurately identify the critical location, a high spatial density of information, *i.e.*, spatially dense strain shapes, is required [5]. However, the conventional approach, using strain sensors, does not provide the required spatial density. In addition to a low spatial density, the presence of a large number of strain sensors changes the structure's response [6]. Non-contact measurement methods have been used to identify the full-field response [7]. One of the most often used approaches is the scanning laser vibrometer [8]; however, this technique requires a stationary process and is time consuming since each location is measured separately [5]. Additionally, the strain response is computed with a double spatial derivation, which significantly increases the noise level [9]. Alternatively, high-speed imaging provides a simultaneous measurement of the entire structure in the field-of-view [10] which allows the research of non-stationary processes and enhances the model identification in frequency [11] and time [12] domains. High-speed imaging techniques have been used for bridge inspections [13], damage assessment [14] and reconstruction of the sound radiation field [15]. Approaches such as a phase-based motion estima-

tion [16] and three-dimensional point-tracking [17] have been used to identify the full-field strain response. Phase-based motion magnification was used in combination with 2D point tracking to enhance the modal parameter identification [18]. A commonly used approach is the Digital Image Correlation (DIC) [19], which has been used successfully for structural health monitoring [20], fatigue testing [21] and damage localization [22]. DIC-based strains have been shown to correlate well with the traditionally used strain sensors for quasi-static, in-plane cases [23]. However, the identification of full-field strain shapes based on a kinematic measurement requires an analytical relation between the kinematics and the stress/strain. For Euler-Bernoulli beam (used in this research), a double spatial derivative is required, which significantly increases the noise.

In contrast to the kinematics-based approach (displacement, velocity, acceleration), taking advantage of the thermoelastic principle [24], the full-field surface stress/strain response of an arbitrary structure can be measured directly. The thermoelastic principle, under the assumption of adiabatic conditions, describes the relation between the thermal emission of the structure and the stress in the material [24]. Using a high-speed infra-red (IR) camera, the high-frequency thermoelastic response (up to several kHz) can be measured. However, the low amplitudes of the thermal emission changes (typically in the range of 1 milliKelvin) in combination with measuring the high-frequency response, generally cause a low signal-to-noise ratio (SNR). Filtering methods such as lock-in correlation [25] have been used to reduce the noise and extract the underlying signal by utilizing the reference signal (usually the measured loading) [26]. While the lock-in correlation has been successfully used to identify the natural frequencies of a plate [27], the periodogram method [28] has been proposed as an efficient alternative to the lock-in correlation. A high-speed IR camera was used to identify the mode shapes of a plate in the frequency range up to 2000 Hz, where each mode was excited separately [29]. The identified shapes showed a good correlation with the shapes from the FE model. As an extension of the modal decomposition method for vibration-fatigue identification [4], the thermoelastic principle has been used to provide the spatial damage-intensity distribution for each of the excited modes [30].

Molina-Viedma *et al.* [29] successfully used the thermoelastic principle to directly identify the strain shapes using an IR camera and estimate their accuracy with respect to a FE model. However, currently it is not known whether the thermoelasticity-based approach is comparable to the kinematics-

based approach and what amplitude of stress/temperature variation is required to achieve strain shapes of comparable accuracy. In this research, the accuracy of the thermoelasticity-based strain shapes of an Euler-Bernoulli beam is evaluated in comparison with the strain shapes obtained from the kinematic measurement. A broadband excitation is used and the strain shapes are obtained from a single measurement. The required amplitude of the stress/temperature variation is determined for two different materials (aluminum and steel) to achieve a strain-shape accuracy comparable to a kinematic measurement. While Euler-Bernoulli beam was used in this research, generalization to arbitrary structures is discussed.

This manuscript is organized as follows. Sec. 2 presents the theoretical background on kinematics-based strain estimations and the thermoelasticity effect. Sec. 3 introduces the methodology for estimating the accuracy of thermoelasticity-based strain shapes. Sec. 4 presents the experimental setup and Sec. 5 presents the results of the study. The conclusions are drawn in Sec. 6.

2. Theoretical background

In this section the theoretical background of the methodology introduced in Sec. 3 will be presented. To compare the kinematics-based strain shapes and the thermoelasticity-based strain shapes, the Euler-Bernoulli beam theory needs to be introduced.

2.1. Estimating strain from kinematics

The surface of a structure is where cracks are most likely to initiate [31]. Therefore, the strain response is typically measured at the surface. In this research, a laser vibrometer is used to measure the velocity of the surface. According to the Euler-Bernoulli beam shown in Fig. 1, the displacements occur in z-direction. The relationship between the kinematic response of the Euler-Bernoulli beam and the strain/stress response is derived.

In the Euler-Bernoulli beam theory [32] the shear strain ε_{xz} is assumed to be zero and its relation to displacements u and w is:

$$\varepsilon_{xz} = \frac{1}{2}\left(\frac{\partial u}{\partial z} + \frac{\partial w}{\partial x}\right) = 0 \tag{1}$$

where the x and z directions are presented in Fig. 1. u is the displacement in the x-direction and w is the displacement in the z-direction. From Eq. (1),

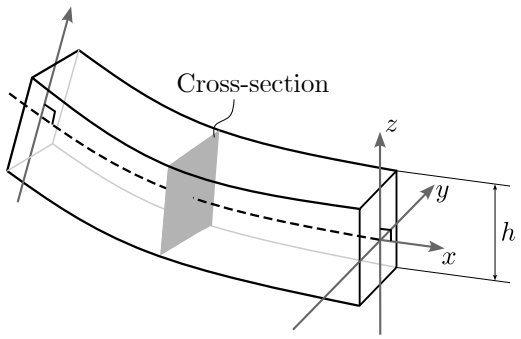

Figure 1: Euler-Bernoulli beam.

the following can be derived:

$$\frac{\partial u}{\partial z} = -\frac{\partial w}{\partial x} \tag{2}$$

Further, the axial displacement in the Euler-Bernoulli beam $u = u(x, z)$ is proportional to the z-coordinate:

$$u = z\,\frac{\partial u}{\partial z} \tag{3}$$

From Eqs. (2) and (3) the following is derived:

$$u = -z\,\frac{\partial w}{\partial x} \tag{4}$$

By inserting Eq. (4) into the definition of normal strain [32], the relation between the displacement of the neutral surface w and the normal strain is derived:

$$\varepsilon_{xx}(z) = \frac{\partial u}{\partial x} = -z\,\frac{\partial^2 w}{\partial x^2} \tag{5}$$

The maximum strain is measured at the surface $\varepsilon_{xx}(z = \frac{h}{2})$, Eq. (5) becomes:

$$\varepsilon_{xx,\max} = \frac{h}{2}\,\frac{\partial^2 w}{\partial x^2}, \tag{6}$$

where h is the thickness of the beam.

When the laser vibrometer is used, the measured velocity must first be integrated with respect to time to obtain the displacements w (can be in

the frequency domain). The FRFs are estimated and the modal parameters (natural frequencies, damping ratios and modal constants) are identified. Then, considering Eq. (6), the second derivative of the modal constants must be calculated with respect to the x-coordinate to estimate the structure's strain modal constants $\mathbf{A}_{\mathrm{L}}^{\varepsilon}$. It is important to note that in case the in-plane displacements of the structure are significant, the measurement location changes and the measured kinematics is not valid.

2.2. Thermoelastic principle for the strain-shape identification

The laws of thermoelasticity describe the relationship between the temperature variations and the elastic stresses in materials [33, 30]. The general law of thermoelasticity is derived from the first law of thermodynamics [34], the laws of continuum mechanics [35] and assumes elastic materials and reversible processes within a closed system [36]:

$$\frac{\mathrm{d}q}{T} = \rho\, C_{\mathrm{p}} \frac{\mathrm{d}T}{T} + \frac{\partial \varepsilon_{ij}}{\partial T} \Delta\sigma_{ij}, \tag{7}$$

where q is the heat transfer from the surrounding environment to the system, ρ is the material's density, C_{p} is the specific heat at constant pressure, ε_{ij} is the strain tensor, and σ_{ij} is the stress tensor [37]. Assuming an adiabatic process ($\mathrm{d}q = 0$), an isotropic material, and plane stress isotropy ($\Delta\sigma_z = 0$), the simplified formulation of thermoelasticity is [33]:

$$\Delta T = K_{\mathrm{m}} \left(\Delta\sigma_x + \Delta\sigma_y \right), \tag{8}$$

where K_{m} is the thermoelastic coefficient [30]:

$$K_{\mathrm{m}} = -\frac{\alpha\, T_0}{\rho\, C_{\mathrm{p}}}, \tag{9}$$

where T_0 is the ambient temperature and α is the thermal expansion coefficient.

The assumption of adiabatic conditions can be made when the speed of heat transfer is significantly lower than the measured vibration frequency, which means that the adiabatic condition is generally satisfied for applications in structural dynamics. Bakis *et al.* [38] showed that, for an aluminum sample, the adiabatic condition can be considered satisfied at frequencies above 5 Hz.

Under normal strain caused by bending, the surface of the material is briefly heated when compressed and cooled when expanded, resulting in temperature variations at the surface. Assuming the elastic response of the vibrating structure and negligible heat dissipation, the process is reversible and the adiabatic condition is satisfied [29]. The IR radiation generated by the high-frequency temperature changes can be measured with a high-speed IR camera. The observed temperature variation is usually expressed in milliKelvin, which is close to the camera's Noise Equivalent Temperature Difference (NETD). Consequently, the IR images are heavily contaminated with noise. NETD, also referred to as thermal constant, defines the minimum temperature difference that the camera can differentiate from the noise [39]. NETD is determined from the standard deviation of the temporal temperature measurement of the temperature controlled black body.

3. Full-field strain response

This section presents the methodology for estimating the strain modal constants using the thermoelastic principle and the methodology to relate the IR camera's accuracy to the strain-identification accuracy.

3.1. Estimating strain modal constants from the IR camera measurement

Each pixel of the IR camera measurement provides a time series of the measured surface temperature. Since the strain FRFs can be estimated using the classical FRF estimators [40], and the relationship between stress changes and temperature changes is linear (8), the temperature data are used to estimate the temperature-based FRFs.

Using the temperature-based FRFs [2] with the Least-Squares Complex Frequency (LSCF) [41] and the Least-Squares Frequency Domain (LSFD) [42] algorithms, the modal parameters are estimated [43]. Due to the high noise level in the IR-camera measurements, the peaks of the FRF at the natural frequencies might be below the noise floor. IR cameras typically specify the noise with the Noise Equivalent Temperature Difference (NETD) value, which will later be used to specify the noise in thermoelastic-based strain identification. In the visual spectrum, a similar limitation was addressed using the hybrid method [43] (combining full-field measurement with high-dynamic range sensor) which is an efficient method of extracting modal data below the noise floor. With the hybrid method, the poles (natural frequencies and damping) are estimated based on a high-dynamic-range sensor (*e.g.*,

accelerometer or laser). The estimated poles are then used with the LSFD to identify the full-field modal constants from the sensor with a high spatial density but low dynamic range, *e.g.*, high-speed camera (more details in [43]). In this research, the hybrid method is researched for the thermoelasticity-based strain EMA. It is expected that the hybrid approach make it possible to identify the full-field strain response at low SNR values.

From the temperature-based FRFs, the temperature modal constants $\mathbf{A}^{\Delta \mathrm{T}}$ are identified; the temperature modal constants $\mathbf{A}^{\Delta \mathrm{T}}$ are related to the strain modal constants $\mathbf{A}^{\varepsilon}$ (8). The strain modal constant is then:

$$\mathbf{A}^{\varepsilon} = \frac{\mathbf{A}^{\Delta \mathrm{T}}}{E\, K_{\mathrm{m}}}, \tag{10}$$

where $\sigma = E\,\varepsilon$ is used, E is the Young's modulus and K_{m} is the thermoelastic, material specific, constant (9). In Eq. (10 it was assumed that $\Delta\sigma_y = 0$, which is a reasonable assumption for a beam [32]. Consequently, $\mathbf{A}^{\varepsilon}$ represents the strains in the x-direction, only. For a beam structure, the relationship between the displacements and the strain is known (5), enabling the kinematics-based strain EMA. The kinematics-based strain EMA, however, cannot be generalized to arbitrary structures. In contrast, the thermoelasticity-based approach can be generalized to an arbitrary structure with a uniaxial response on the surface. For structures with multiaxial response, because the temperature change ΔT is related to $\Delta\sigma_x + \Delta\sigma_y$, see Eq. (8), the x and y components cannot be arbitrarily separated in the resulting stress/strain modal constants.

The strain modal shape at location j is defined as [44]:

$$\phi_j^{\varepsilon} = \frac{A_j^{\varepsilon}}{\phi_k} \tag{11}$$

where A_j^{ε} is the strain modal constant at the j-th location and ϕ_k is the modal shape at the driving point k (a single excitation location is assumed). The ratio between A_j^{ε} and ϕ_j^{ε} is constant regardless of the observed location j. Thus, the shapes of $\mathbf{A}^{\varepsilon}$ and ϕ^{ε} are identical, differing only in amplitude [44].

3.2. Thermoelasticity-based strain-response accuracy

To validate the use of the thermoelastic principle for strain modal analysis and to estimate its accuracy with respect to the kinematic-based measurements, the thermoelasticity-based strain modal constants $\mathbf{A}_{\mathrm{C}}^{\varepsilon}$ are compared

to the kinematics-based strain modal constants $\mathbf{A}_{\mathrm{L}}^{\varepsilon}$. The Modal Assurance Criterion (MAC) [45] is used as a measure of the correlation between the two. The MAC value between the r-th kinematics-based strain modal constant ${}_r\mathbf{A}_{\mathrm{L}}^{\varepsilon}$ and the r-th thermoelasticity-based strain modal constant ${}_r\mathbf{A}_{\mathrm{C}}^{\varepsilon}$ is defined as:

$$\mathrm{MAC} = \frac{|{}_r\mathbf{A}_{\mathrm{L}}^{\varepsilon T} \cdot {}_r\mathbf{A}_{\mathrm{C}}^{\varepsilon}|^2}{({}_r\mathbf{A}_{\mathrm{C}}^{\varepsilon T} \cdot {}_r\mathbf{A}_{\mathrm{L}}^{\varepsilon})\,({}_r\mathbf{A}_{\mathrm{L}}^{\varepsilon T} \cdot {}_r\mathbf{A}_{\mathrm{C}}^{\varepsilon})}, \tag{12}$$

where ^{T} denotes the transpose of the vector and $|\cdot|$ denotes taking the absolute value. The MAC value for a pair of modal shapes/constants is unity if one shape is a scalar multiple of the other and zero if there is no correlation between the two shapes [46]. In the experimental research (Sec. 4), the MAC values are computed between the matching kinematics-based (laser vibrometer) strain modal constants, identified under optimal excitation conditions, and thermoelasticity-based (IR camera) strain modal constants, identified under increasing excitation amplitudes.

At small excitation amplitudes, the temperature time series from the IR camera are contaminated with noise. The excitation amplitude (and consequently the surface temperature amplitude) is sequentially increased to establish the relationship between the measured temperature amplitude ΔT at a selected natural frequency, and the accuracy of the corresponding thermoelasticity-based strain modal constant $\mathbf{A}_{\mathrm{C}}^{\varepsilon}$. The minimum required temperature amplitude is then determined, at which the full-field strain modal constants (with an accuracy comparable to the kinematics-based approach under optimal conditions) can be identified from a single measurement without smoothing.

4. Experimental research

To compare the thermoelasticity-based and kinematics-based strain modal constants an experiment was set up and the data were acquired using the IR camera and laser vibrometer.

4.1. Experimental setup

Aluminum and steel beams with dimensions of 415 mm × 20 mm × 3 mm were suspended using strings to simulate free-free boundary condition. The strings were glued to the top of the beams to enable an uninterrupted full-field measurement. The beams were excited by an electro-dynamic shaker, model LDS V555, mounted in a horizontal position, see Fig. 2. The fronts

of the beams were painted with a high emissivity, low reflectivity black paint (Thermo Special by Motip) to enhance the thermoelastic effect and minimize the IR reflections of the environment. In addition to the black paint, a highly reflective sticker was placed on the top part of the beam's front face, which was needed for the laser measurement. The sticker was present during the entire experiment to ensure an identical structure for both the IR camera and laser measurements. The excitation force at the stinger was measured with a Dytran 1022V force sensor, see Fig. 2. A pseudo-random signal in the range from 20 Hz to 2500 Hz was generated [47] and was amplified by the LDS PA1000L amplifier.

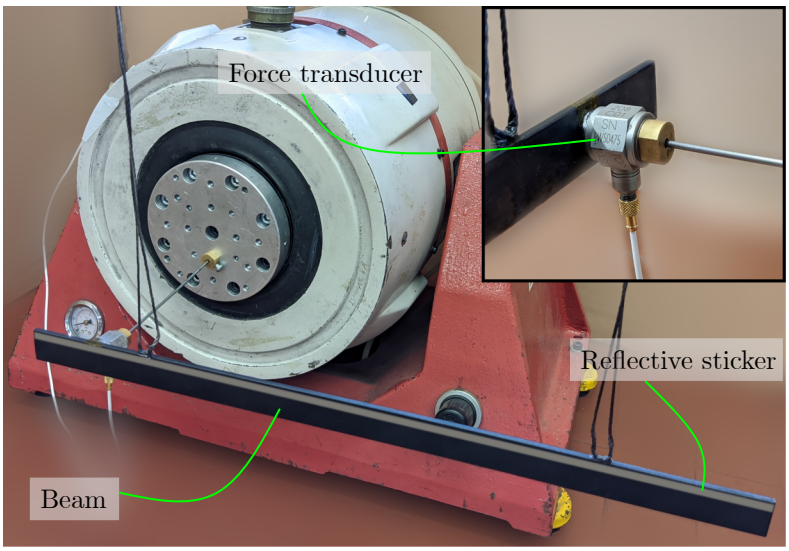

Figure 2: Experimental setup (beam and shaker).

4.2. Thermal camera measurement

The Telops FAST m3K high-speed thermal imaging camera (Fig. 3) was used to measure the temperature variations on the surface of the beam. The Noise Equivalent Temperature Difference (NETD) of the camera is 32 milliKelvin. The camera uses 16-bit encoding. A resolution of 320×20 pixels was used, with a frame rate of 5000 frames per second. The sampling frequency for the excitation force was 25600 Hz. To synchronize the camera and the measurement of the excitation force, a trigger signal was used to simultaneously trigger the camera and the acquisition of the force. The

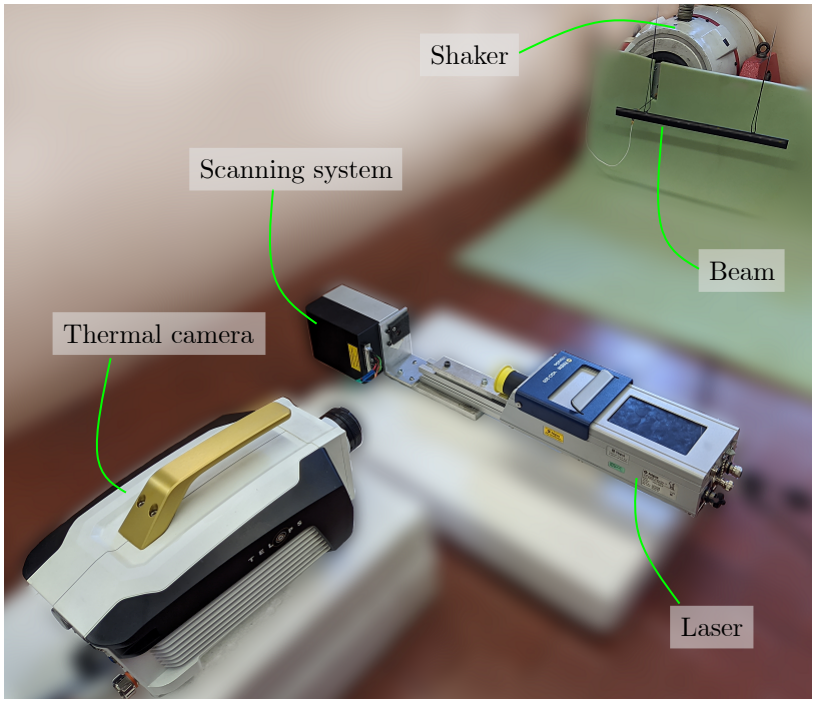

Figure 3: Laser, thermal camera, beam and shaker setup.

duration of the image sequence and force acquisition was 5 seconds. Because all signal processing is done in the frequency domain, the difference in the sampling frequency does not present an issue. The measurement duration is equal for both thermal camera and force (5 seconds), therefore the frequency resolution for thermal camera and force is also equal (1/5 Hz).

To investigate the effect of the excitation amplitude on the temperature variation amplitudes ΔT on the surface of the beam and the identification of the strain modal constants $\mathbf{A}_{\mathrm{C}}^{\varepsilon}$, the excitation amplitude was increased sequentially.

Fig. 4 shows the thermoelasticity-based strain modal constant estimation process. The temperature time series of each pixel was transformed into the frequency domain and the FRFs were estimated (the Welch method with a 50% Hann window function overlap was used). The frequency resolution of the FRF was 1 Hz. The hybrid method [43] was used to identify the thermoelasticity-based strain modal constants; the poles (natural frequencies and damping) were identified from the laser measurement at a single location. To obtain the real-valued modal constants, proportional damping

was assumed in the LSFD algorithm [42]. The full-field strain modal constants (Fig. 5) were averaged in the vertical direction of the beam (Fig. 4), reducing the noise but not the spatial resolution. It is worth mentioning that the peak in the FRF at 50 Hz (Fig. 4b) is a consequence of the electrical grid frequency.

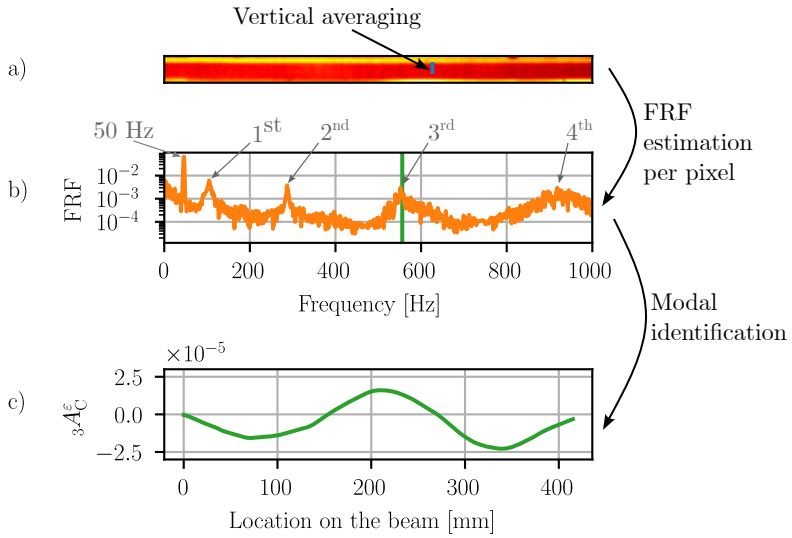

Figure 4: a) camera frame, b) frequency response function and c) full-field strain modal constant ${}_3\mathbf{A}^{\varepsilon}_{\mathrm{C}}$ of 3rd mode.

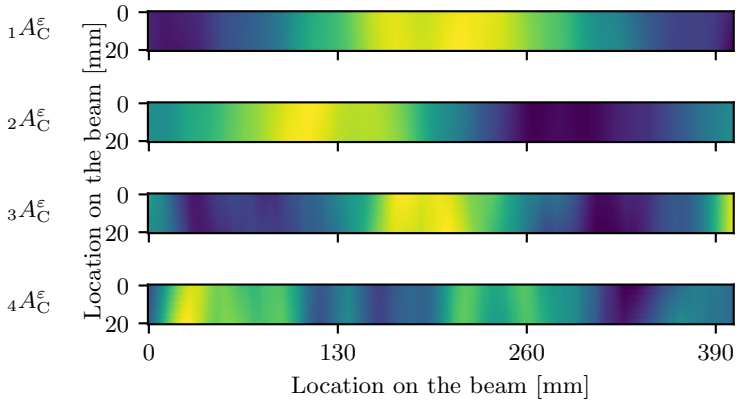

Figure 5: First four full-field thermoelasticity-based strain modal constants $\mathbf{A}^{\varepsilon}_{\mathrm{C}}$.

4.3. Laser vibrometer measurement

The response of the structure was also measured using the laser vibrometer. A Polytec VGO-200 laser with a 2-axis mirror was used (Fig. 3) to move the measurement point along the length of the beam and obtain the full-field response. The response was determined at 320 points along the entire length of the beam in order to obtain the same (longitudinal) density of information as with the thermal camera. The sampling frequency for the force sensor and the laser (velocity) measurement was 25600 Hz. The force and velocity measurements were triggered simultaneously; however, the laser has a time delay of $\Delta t = 292\,\mu$s (provided by the manufacturer and experimentally confirmed), which was compensated in the frequency domain [48]:

$$\mathcal{F}[x(t-\Delta t)] = \mathcal{F}[x(t)] \cdot \exp\left(2\pi \mathrm{i} f \Delta t\right) \tag{13}$$

where $\mathcal{F}[x(t)]$ denotes the Fourier transformation of $x(t)$ to the frequency domain, f is the frequency in Hz, and $\mathrm{i} = \sqrt{-1}$. The measurement at each point lasted for 5 seconds.

LSCF and LSFD algorithms were used to identify the modal constants from the laser measurements and double spatial derivation (6) with a moving average (with a window length of 53) was performed to estimate the strain modal constants. The moving average was chosen for filtering since it is the most basic and predictable filter. Fig. 6 shows the estimation of the strain modal constants by a derivation of the raw data (from 6a) to 6b) and 6d)), and a derivation with a moving average applied (from 6a) to 6c) and 6e)). When comparing Fig. 6d) and 6e) it is clear that smoothing must be applied to obtain distinguishable strain modal constants $\mathbf{A}^{\varepsilon}_{\mathrm{L}}$. Note that because of the moving average, the first and last $(53-1)/2 = 26$ points were not calculated correctly (zero padding was used); however, in Fig. 6 all 320 points are shown regardless. When calculating the MAC values (Sec. 5), only $320-4\cdot 26 = 216$ were taken into account (moving average was applied twice), to exclude the boundary effect. Further, it is important to emphasize that the thermoelasticity-based modal constants provide accurate information at the edges of the beam and do not require truncation since no moving average is used.

4.4. Strain-sensor measurement

In order to reliably identify the thermoelastic constant K_{m} needed to estimate the stress based on a measured temperature (8), a separate experiment

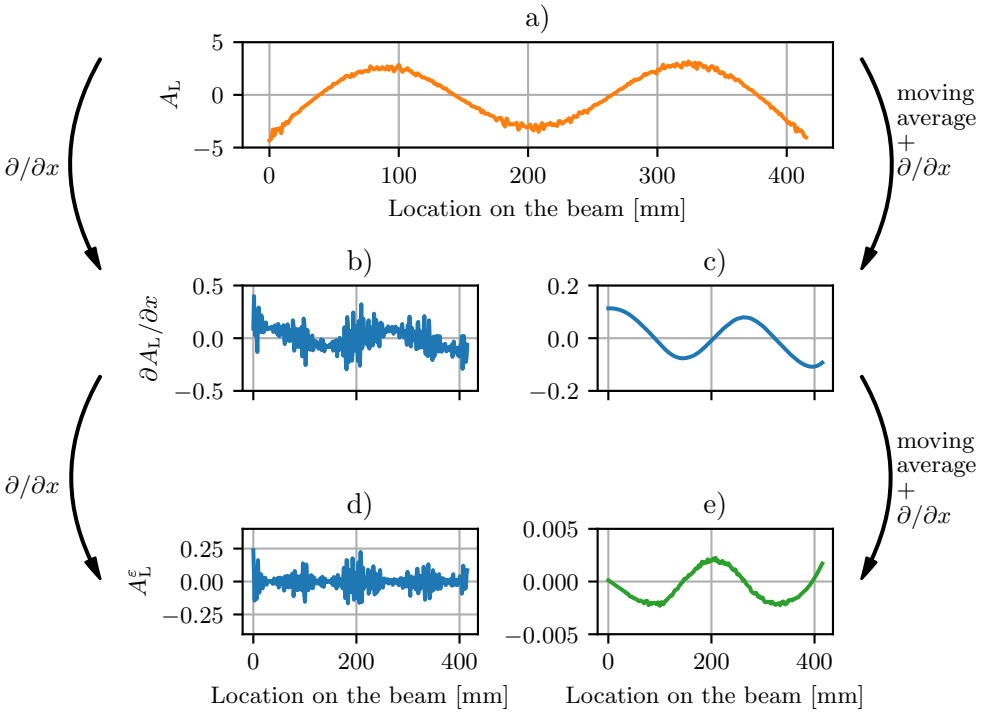

Figure 6: Estimation of strain modal constant $\mathbf{A}_{\mathrm{L}}^{\varepsilon}$ from laser measurement without smoothing (from a) to b) and d)) and with smoothing (from a) to c) and e)).

was carried out using a combination of strain sensor and IR camera. A PCB 740B02 strain sensor was placed 150 mm from the edge of the beam (on the back side of the beam) and a harmonic signal (230 Hz and 350 Hz for the aluminum and steel beams, respectively) was generated to excite the structure. Simultaneously, the response of the front of the beam was measured using the IR camera at the strain sensor's location. The procedure of K_{m} identification is described in Appendix A. The required material properties and the identified thermoelastic coefficients are presented in Tab. 1.

Table 1: Material properties and identified K_{m}.

Material	Young's modulus E [GPa]	Poisson's ratio ν [/]	K_{m} [°C/Pa]
Aluminum	72	0.3	$1.98 \cdot 10^{-9}$
Steel	193	0.3	$3.16 \cdot 10^{-10}$

5. Results and discussion

To evaluate the accuracy of the results, the thermoelasticity-based strain modal constants $\mathbf{A}_{\mathrm{C}}^{\varepsilon}$ were compared with the kinematics-based (laser) strain modal constants $\mathbf{A}_{\mathrm{L}}^{\varepsilon}$. The MAC values were calculated for five identified natural frequencies at an increasing excitation amplitude (in each iteration the excitation-force RMS was increased by approximately 1 N and 5 N for aluminum and steel beams, respectively). The reference laser-based measurement was performed at an excitation level with a high SNR. It is important to emphasize at this point that the laser-based measurement is sequential and takes approximately one hour (depending on the measurement time at each point), while a thermoelasticity-based measurement acquires all the measurement locations simultaneously in a 5-second measurement. For both laser and thermal-camera measurements, no repeating measurements for averaging were performed during the experiment. In the post-processing phase, the Welch method was used.

The MAC values for the first strain modal constant ${}_1\mathbf{A}^{\varepsilon}$ at an increasing excitation amplitude are shown in Fig. 7. The aluminum and steel samples were tested at 14 and 11 different excitation levels, respectively. With increasing excitation-force RMS value the correlation between the laser strain modal constant ${}_1\mathbf{A}_{\mathrm{L}}^{\varepsilon}$ and the IR camera strain modal constant ${}_1\mathbf{A}_{\mathrm{C}}^{\varepsilon}$ improves significantly. This is true for both the aluminum and steel beams. From Fig. 7 and the analysis of higher modes, it can be concluded that it is crucial to maintain a sufficiently high level of excitation, particularly for components with a reduced thermal response. However, the excitation-force RMS criterion cannot be generalized to an arbitrary structure because the response to excitation depends on the FRF of the structure. In addition, the RMS value does not contain information about the frequency content, which has a significant influence on whether a particular mode is sufficiently excited. For these reasons, research has focused on the response amplitude rather than the excitation amplitude.

Thermoelasticity-based strain modal constants $\mathbf{A}_{\mathrm{C}}^{\varepsilon}$ are determined from the temperature-based modal constants $\mathbf{A}_{\mathrm{C}}^{\Delta T}$ (10). Because $\mathbf{A}_{\mathrm{C}}^{\Delta T}$ are identified based on the measured temperature, see Sec. 3.1, a sufficiently large response temperature is required to achieve a satisfactory accuracy of $\mathbf{A}_{\mathrm{C}}^{\varepsilon}$. To research the response surface temperature, the average surface-temperature amplitude of the i-th mode ${}_i\overline{\Delta T}$ needs to be defined. ${}_i\overline{\Delta T}$ is the average of all locations (pixels) of the surface-temperature amplitude at the i-th natural

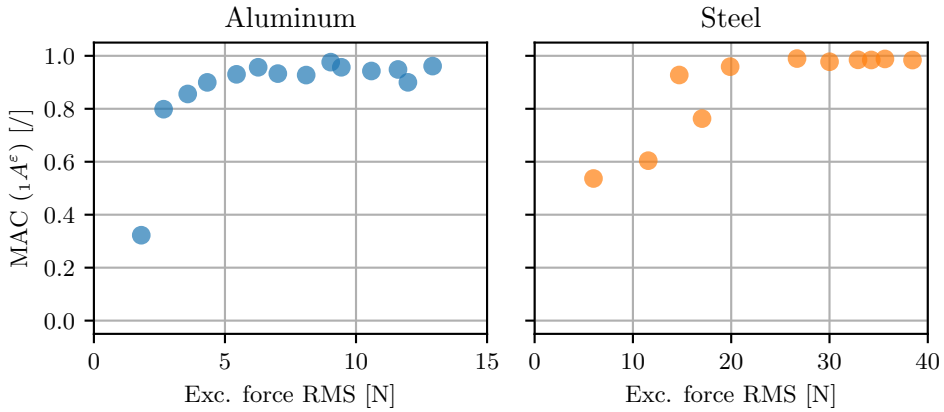

Figure 7: MAC values for first strain modal constant at increasing excitation amplitudes.

frequency. Fig. 8 shows the MAC values versus $_i\overline{\Delta T}$; where the normalization to the NETD property of the camera is used to remove the dependence on the IR camera. Fig. 8 shows $_i\overline{\Delta T}$/NETD for five modes at 14 and 11 excitation levels for the aluminum and steel samples, respectively. The different modes are deliberately not marked to show more clearly the dependence of the MAC values on the response amplitudes. From the $(14+11)\times 5 = 125$ experimental results it is clear that at approximately $_i\overline{\Delta T}$/NETD=0.006 the MAC values show a good correlation with the reference laser-based experiment. Since the geometry and material properties of the structure do not affect the relationship in Fig. 8, the identified threshold value, $_i\overline{\Delta T}$/NETD = 0.006, can be directly applied to an arbitrary structure (see Sec. 3.1 for details regarding structures with uniaxial and multiaxial response).

As can be seen from the Fig. 8, due to the hybrid method [43], successful identification of the modal shapes at relatively small response amplitudes close to the noise floor ($_i\overline{\Delta T}$/NETD = 0.004) is possible. The noise floor shown in Fig. 8 and Fig. 9 was estimated by computing the amplitude spectrum of the temperature measurement from the thermal camera. The highest 10% of amplitudes of the frequency ranges where the spectrum appeared flat were averaged. If the hybrid method was not used, significantly higher surface temperatures would be required: without the hybrid method, the stabilization of the poles from the temperature FRFs (Fig. 4b)) was successful for the first mode at the largest excitation level (for both tested materials), only. Consequently, without the hybrid method, only the first mode $_1\mathbf{A}_\mathrm{C}^\varepsilon$ was

identified with a MAC value of approximately 0.8. The hybrid method is therefore essential for an accurate thermoelastic-based full-field strain modal constant identification.

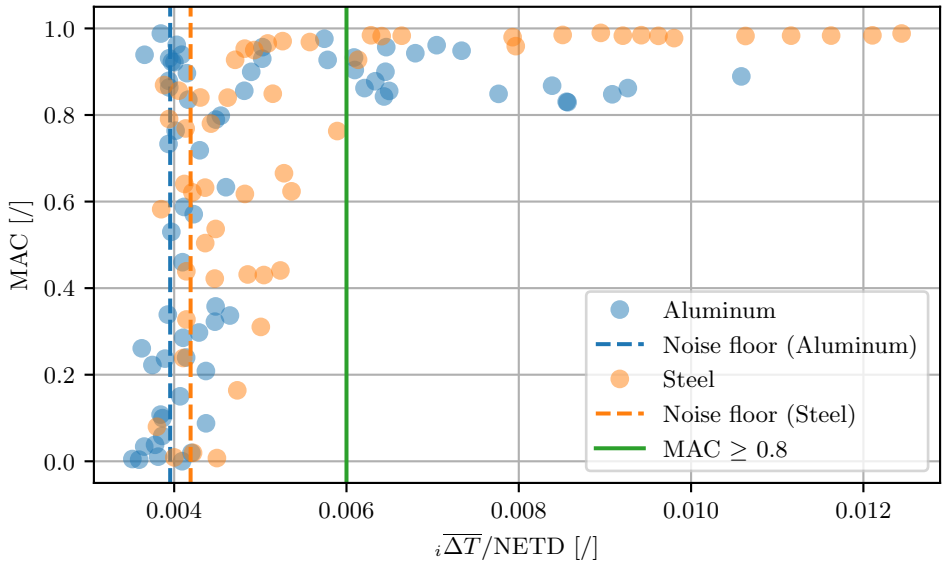

Figure 8: MAC values with respect to the surface temperature variation amplitudes (normalized to NETD).

$_i\overline{\Delta T}/\mathrm{NETD} = 0.006$ is a very important finding of this research. However, in the design phase of an experiment it is difficult to predict the amplitude of the averaged surface temperature of the i-th mode $_i\overline{\Delta T}$, while the estimation of the surface stress amplitude of the i-th mode $_i\overline{\Delta\sigma}$ can be obtained from numerical simulations. Consequently, the $_i\overline{\Delta\sigma}$ will here be related to $_i\overline{\Delta T}$ by using the thermoelastic coefficients K_m, see Tab. 1, and Eq. (8). In Fig. 9, the MAC values from Fig. 8 are shown as a function of $_i\overline{\Delta\sigma}$. The MAC value between $\mathbf{A}^{\varepsilon}_{\mathrm{C}}$ and $\mathbf{A}^{\varepsilon}_{\mathrm{L}}$ is greater than 0.8 when the average surface stress amplitude at the natural frequency $_i\overline{\Delta\sigma}$ exceeds approx. 100 kPa and approx. 500 kPa for the aluminum and steel, respectively.

6. Conclusions

The use of the thermoelastic principle makes it possible to measure the full-field strain shapes directly; however, the accuracy and identification lim-

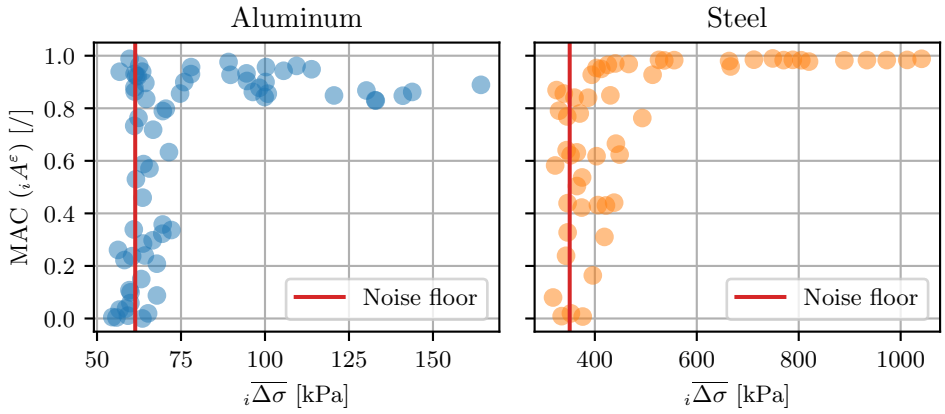

Figure 9: MAC values with respect to the surface stress variation amplitudes $_i\overline{\Delta\sigma}$.

itations have not been researched in the context of recent progress in the field of high-speed camera-based measurements (e.g., the hybrid EMA method).

This research introduces the hybrid method to the identification of IR-camera-based strain EMA, where a laser vibrometer measurement was used for the pole identification and an IR-camera measurement for the strain modal constants identification. In the experimental research it was shown that the IR-camera approach was successful in identifying the strain modal parameters of the first mode, only. Using the hybrid method, five thermoelasticity-based strain modal constants were identified at response amplitudes even below the noise floor. The hybrid approach was shown to be essential for the identification of strain amplitudes below the noise floor of the IR-camera.

Additionally, the accuracy of thermoelastic-based strain EMA was researched with regard to the IR-camera measurement noise, typically specified via the NETD (Noise Equivalent Temperature Difference) value. First, it was found that the surface-temperature amplitude, normalized to NETD, needs to exceed 0.006 for a successful thermoelastic stain EMA identification (MAC>0.8). Second, the normalized temperature amplitude was related to the surface stress (via the thermoelastic coefficient); it was found that amplitudes of surface stress of approximately 100 kPa and 500 kPa result in successful thermoelastic strain EMA identification for aluminum and steel, respectively.

In contrast to a laser measurement, where sequential measurements can last hours, the thermoelasticity-based (IR-camera) strain modal parameters

were identified from a single response measurement. With the identified thermoelasticity-based full-field strain modal response, accurate identification of critical damage locations and full-field damage-intensity maps is feasible.

Acknowledgment

The authors acknowledge partial financial support from the Slovenian Research Agency (research core funding No. P2-0263 and research project N2-0144).

Appendix A. Thermoelastic constant estimation

The thermoelastic constant K_{m} was estimated based on the strain-sensor and IR-camera measurements. A harmonic excitation signal was generated for the aluminum and steel beams at 230 and 350 Hz, respectively. The frequencies were selected to ensure a high response of the beam at the strain-sensor location. Both the strain and temperature (at the location of the strain sensor) signals were transformed to the frequency domain and proper scaling of the amplitude was ensured. The thermoelastic constant was then estimated [30]:

$$K_{\mathrm{m}} = \frac{\Delta T(f_0)\,(1-\nu)}{\Delta\varepsilon(f_0)\,E}, \tag{A.1}$$

where E is the Young's modulus, ν is the Poisson's ratio, $\Delta T(f_0)$ is the temperature amplitude at the frequency f_0 and $\Delta\varepsilon(f_0)$ is the strain amplitude at f_0. f_0 was 230 and 350 Hz for the aluminum and steel beams, respectively.

The identified thermoelastic constants K_{m} and the required material properties are presented in Tab. 1.

References

[1] L. H. Yam, T. P. Leung, D. B. Li, and K. Z. Xue. Theoretical and experimental study of modal strain analysis. *Journal of Sound and Vibration*, 191(2):251–260, 3 1996.

[2] D.J. Ewins. *Modal Testing: Theory, Practice and Application*. 2009.

[3] Yadong Zhou and Jiayue Tao. Theoretical and numerical investigation of stress mode shapes in multi-axial random fatigue. *Mechanical Systems and Signal Processing*, 127:499–512, 7 2019.

[4] Matjaž Mršnik, Janko Slavič, and Miha Boltežar. Vibration fatigue using modal decomposition. *Mechanical Systems and Signal Processing*, 98:548–556, 1 2018.

[5] Kedar Bharadwaj, Azadeh Sheidaei, Arash Afshar, and Javad Baqersad. Full-field strain prediction using mode shapes measured with digital image correlation. *Measurement*, 139:326–333, 6 2019.

[6] Chunyan Ao, Baijie Qiao, Meiru Liu, Weidong Zhu, Yuda Zhu, Yanan Wang, and Xuefeng Chen. Non-contact full-field dynamic strain reconstruction of rotating blades under multi-mode vibration. *Mechanical Systems and Signal Processing*, 186:109840, 3 2023.

[7] Alessandro Zanarini. Competing optical instruments for the estimation of Full Field FRFs. *Measurement*, 140:100–119, 7 2019.

[8] Yuanchang Chen and D. Todd Griffith. Experimental and numerical full-field displacement and strain characterization of wind turbine blade using a 3D Scanning Laser Doppler Vibrometer. *Optics & Laser Technology*, 158:108869, 2 2023.

[9] Rick Chartrand. Numerical Differentiation of Noisy, Nonsmooth Data. *ISRN Applied Mathematics*, 2011:1–11, 5 2011.

[10] Jaka Javh, Janko Slavič, and Miha Boltežar. The subpixel resolution of optical-flow-based modal analysis. *Mechanical Systems and Signal Processing*, 88:89–99, 2017.

[11] Klemen Zaletelj, Janko Slavič, and Miha Boltežar. Full-field DIC-based model updating for localized parameter identification. *Mechanical Systems and Signal Processing*, 164, 2 2022.

[12] Thijs Willems, Felix Simeon Egner, Yonggang Wang, Matteo Kirchner, Wim Desmet, and Frank Naets. Time-domain model identification of structural dynamics from spatially dense 3D vision-based measurements. *Mechanical Systems and Signal Processing*, 182:109553, 1 2023.

[13] Tengjiao Jiang, Gunnstein Thomas Frøseth, and Anders Rønnquist. A robust bridge rivet identification method using deep learning and computer vision. *Engineering Structures*, 283:115809, 5 2023.

[14] Hao Hu, Jiji Wang, Chuan-Zhi Dong, Jiaqi Chen, and Tao Wang. A hybrid method for damage detection and condition assessment of hinge joints in hollow slab bridges using physical models and vision-based measurements. *Mechanical Systems and Signal Processing*, 183:109631, 1 2023.

[15] P. Gardonio, G. Guernieri, E. Turco, L. Dal Bo, R. Rinaldo, and A. Fusiello. Reconstruction of the sound radiation field from flexural vibration measurements with multiple cameras. *Mechanical Systems and Signal Processing*, 195:110289, 7 2023.

[16] Yongchao Yang, Hwee-Kwon Jung, Charles Dorn, Gyuhae Park, Charles Farrar, and David Mascareñas. Estimation of full-field dynamic strains from digital video measurements of output-only beam structures by video motion processing and modal superposition. *Structural Control and Health Monitoring*, 26(10), 10 2019.

[17] Javad Baqersad, Peyman Poozesh, Christopher Niezrecki, and Peter Avitabile. A Noncontacting Approach for Full-Field Strain Monitoring of Rotating Structures. *Journal of Vibration and Acoustics*, 138(3), 6 2016.

[18] Marc Eitner, Benjamin Miller, Jayant Sirohi, and Charles Tinney. Effect of broad-band phase-based motion magnification on modal parameter estimation. *Mechanical Systems and Signal Processing*, 146:106995, 1 2021.

[19] W. H. Peters and W. F. Ranson. Digital Imaging Techniques In Experimental Stress Analysis. *Optical Engineering*, 21(3):213427, 6 1982.

[20] Christopher Niezrecki, Javad Baqersad, and Alessandro Sabato. Digital Image Correlation Techniques for NDE and SHM. In *Handbook of Advanced Non-Destructive Evaluation*, pages 1–46. Springer International Publishing, Cham, 2018.

[21] Benjamin D Hill, Brandon A Furman, Emma E German, Jacob R Rigby, and Ryan B Berke. Non-contact strain measurement to eliminate strain gages in vibration-based high cycle fatigue testing. *The Journal of Strain Analysis for Engineering Design*, 58(2):141–156, 2 2023.

[22] Shancheng Cao, Haibo Nian, Jinwei Yan, Zhiwen Lu, and Chao Xu. Modal analysis and damage localization in plate-type structures via TDD and PE methods based on the data of an integrated highspeed camera system. *Mechanical Systems and Signal Processing*, 178:109309, 10 2022.

[23] Jennifer Carr, Javad Baqersad, Christopher Niezrecki, Peter Avitabile, and Micheal Slattery. Dynamic Stress–Strain on Turbine Blades Using Digital Image Correlation Techniques Part 2: Dynamic Measurements. In *Topics in Experimental Dynamics Substructuring and Wind Turbine Dynamics, Volume 2*, pages 221–226. Springer New York, New York, NY, 2012.

[24] G Pitarresi and E. A Patterson. A review of the general theory of thermoelastic stress analysis. *The Journal of Strain Analysis for Engineering Design*, 38(5):405–417, 7 2003.

[25] G. Pitarresi. Lock-In Signal Post-Processing Techniques in Infra-Red Thermography for Materials Structural Evaluation. *Experimental Mechanics*, 55(4):667–680, 4 2015.

[26] Ralf Urbanek and Jürgen Bär. Lock-In Thermographic Stress Analysis of notched and unnotched specimen under alternating loads. *Procedia Structural Integrity*, 5:785–792, 2017.

[27] Zuzana Stankovičová, Vladimír Dekýš, Pavol Novák, and Bohumír Strnadel. Detection of Natural Frequencies Using IR Camera. *Procedia Engineering*, 192:830–833, 2017.

[28] A.J. Molina-Viedma, L. Felipe-Sesé, E. López-Alba, and F.A. Díaz. Comparison of lock-in correlation and a novel periodogram method for experimental multi-harmonic thermoelastic analysis. *Mechanical Systems and Signal Processing*, 164:108235, 2 2022.

[29] Ángel J. Molina-Viedma, Luis Felipe-Sesé, Elías López-Alba, and Francisco A. Díaz. Thermoelastic effect in modal shapes at high frequencies using infrared thermography. *Measurement: Journal of the International Measurement Confederation*, 176, 5 2021.

[30] Lorenzo Capponi, Janko Slavič, Gianluca Rossi, and Miha Boltežar. Thermoelasticity-based modal damage identification. *International Journal of Fatigue*, 137, 8 2020.

[31] Michael D. Sangid. The physics of fatigue crack initiation. *International Journal of Fatigue*, 57:58–72, 12 2013.

[32] Bauchau O. A. and J I Craig. Euler-Bernoulli beam theory. In J I Bauchau O. A.Craig, editor, *Structural Analysis*, pages 173–221. Springer Netherlands, Dordrecht, 2009.

[33] William Thomson. XV. On the Dynamical Theory of Heat, with numerical results deduced from Mr Joule's Equivalent of a Thermal Unit, and M. Regnault's Observations on Steam. *Transactions of the Royal Society of Edinburgh*, 20(2):261–288, 1853.

[34] Peter Atkins. *The laws of thermodynamics: A very short introduction*. OUP Oxford, 2010.

[35] Anthony James Merrill Spencer. *Continuum mechanics*. Courier Corporation, 2004.

[36] A. K. Wong, J. G. Sparrow, and S. A. Dunn. On the revised theory of the thermoelastic effect. *Journal of Physics and Chemistry of Solids*, 49(4):395–400, 1 1988.

[37] William N Sharpe. *Springer handbook of experimental solid mechanics*. Springer Science & Business Media, 2008.

[38] Charles E. Bakis and Kenneth L. Reifsnider. The adiabatic thermoelastic effect in laminated fiber composites. *Journal of Composite Materials*, 25:809–830, 7 1991.

[39] Craig Hoffman and Ronald Driggers, editors. *Encyclopedia of Optical and Photonic Engineering, Second Edition*. CRC Press, 9 2015.

[40] Nuno M M Maia and J M Montalvão e Silva. *Theoretical and Experimental Modal Analysis*. John Wiley & Sons, 1997.

[41] P Guillaume, L. Hermans, and H. Van der Auwerer. Maximum Likelihood Identification of Modal Parameters from Operational Data. *Proceedings of the 17th International Modal Analysis Conference (IMAC17)*, pages 1887–1893, 1999.

[42] Bart Cauberghe. *Applied frequency-domain system identification in the field of experimental and operational modal analysis*. PhD thesis, Vrije Universiteit Brussel, 2004.

[43] Jaka Javh, Janko Slavič, and Miha Boltežar. High frequency modal identification on noisy high-speed camera data. *Mechanical Systems and Signal Processing*, 98:344–351, 2018.

[44] Tadej Kranjc, Janko Slavič, and Miha Boltežar. A comparison of strain and classic experimental modal analysis. *JVC/Journal of Vibration and Control*, 22(2):371–381, 2016.

[45] R. J. Allemang and D. L. Brown. A correlation coefficient for modal vector analysis. *Proceedings of the first international Modal Analysis Conference*, pages 110–116, 1982.

[46] Randall J Allemang. The modal assurance criterion - Twenty years of use and abuse. *Sound and Vibration*, 37(8):14–21, 2003.

[47] Aleš Zorman, Domen Gorjup, and Janko Slavič. ladisk/pyExSi: Release of the version v0.4, 2021.

[48] Kihong Shin and Joseph Hammond. *Fundamentals of Signal Processing for Sound and Vibration Engineers*. 2008.